JOURNAL OF THERMOPHYSICS AND HEAT TRANSFER
Vol. 21, No. 3, July–September 2007

# Analysis of Screen Wick Heat Pipes, Including Capillary Dry-Out Limitations

Jeremy Rice* and Amir Faghri†
*University of Connecticut, Storrs, Connecticut 06269-3139*

DOI: 10.2514/1.24809

**A complete numerical analysis of heat pipes is performed with no empirical correlations while including the flow in a wick. The numerical model is validated from experimental and numerical work. Single and multiple heat sources were used as well as constant, convective, and radiative heat sinks. The numerical model does not fix the internal pressure references by a point, but allows it to rise and fall based on the physics of the problem. Also, the capillary pressure needed in the wick to drive the flow is obtained for various heating configurations and powers. These capillary pressures, in conjunction with an analysis that predicts the maximum capillary pressure for a given heating load, are used to determine the dry-out limitations of a heat pipe.**

## Nomenclature

$f$ = friction factor
$h$ = enthalpy, J/kg
$h_{\mathrm{fg}}$ = latent heat of vaporization, J/kg
$\mathbf{I}$ = identity matrix
$\mathbf{K}$ = permeability tensor, m$^2$
$\dot{m}''$ = evaporative mass flux, kg/s $\cdot$ m$^2$
$\mathbf{n}$ = unit normal vector
$p$ = pressure, Pa
$Q$ = heat in
$r$ = radial direction, m
$T$ = temperature, K
$TC$ = thermal capacity of the heat pipe, J/°C
$t$ = time, s
$\mathbf{t}$ = unit tangent vector
$u$ = $x$ velocity, m/s
$V$ = elementary volume, m$^3$
$\mathbf{V}$ = velocity vector, m/s
$v$ = radial or $y$ velocity, m/s
$\mathbf{v}$ = volume averaged velocity, m/s
$w$ = $z$ velocity, m/s
$x$ = Cartesian or axial coordinate, m
$y$ = Cartesian coordinate, m
$z$ = Cartesian coordinate, m
$\Delta T$ = change in temperature, K
$\Delta t$ = time step size, s
$\Delta x$ = distance a section spans, m
$\varepsilon$ = emmisivity
$\Theta$ = general variable
$\lambda$ = heat transfer coefficient, W/m$^2$ $\cdot$ K
$\mu$ = dynamic viscosity, N $\cdot$ s/m$^2$
$\rho$ = density, kg/m$^3$
$\sigma$ = Stefan–Boltzmann constant
$\boldsymbol{\tau}$ = stress tensor, N/m$^2$
$\Phi$ = viscous dissipation, W/m$^3$
$\varphi$ = porosity

*Subscripts*

$c$ = cooled section, condenser, coolant
$f$ = fluid
$h$ = heated section, evaporator
in = referring to heat input
$l$ = liquid
$m$ = center of a heated or cooled section
out = referring to heat output
$s$ = solid
stor = storage
tot = total heat input
$v$ = vapor
$w$ = wick

## I. Introduction

HEAT pipes are one of the most efficient ways to transport heat [1]. They use evaporation and condensation, and the natural pumping capability of a wick structure, and therefore can transport heat over relatively large distances, with small temperature drops without the use of external power to pump the fluid. Heat pipes can operate at a wide range of temperatures and heating loads, based on their design. Because heat pipes have a wide operating range, they can be applied to several areas including the cooling of electronic equipment and high performance space applications as well as the cooling of nuclear isotope reactors. In addition to convectional cylindrically shaped heat pipes, flat-plate heat pipes (FPHP) have recently received attention because of their ability to dissipate heat in localized regions as is necessary in many electronic cooling applications.

Faghri and Buchko [2] experimentally and numerically investigated the operating performance of low-temperature cylindrical heat pipes with multiple heat sources. They used a cylindrical heat pipe with a screen wick, with four independently controlled wrapped heaters. They experimentally determined when “dry out” would occur in the wick when the heat load was increased in several different arrangements. The numerical model was solved by using a transformation of the Navier–Stokes and energy equations into a single domain problem.

High-temperature cylindrical heat pipes were investigated by Cao and Faghri [3]. They numerically modeled the compressibility effects in the vapor region and modeled the wick as a solid region with an effective heat capacity and thermal conductivity. The transient effects were modeled as a step change in the applied heat flux, with convective and radiative boundary conditions.

A network model of a heat pipe was proposed by Zuo and Faghri [4] that modeled the transient heat pipe behavior as a first order, linear, ordinary differential equation (ODE). They developed a nondimensional number, which is a quantification of the geometrical

---

Received 1 May 2006; revision received 3 October 2006; accepted for publication 4 October 2006. Copyright © 2006 by the American Institute of Aeronautics and Astronautics, Inc. All rights reserved. Copies of this paper may be made for personal or internal use, on condition that the copier pay the $10.00 per-copy fee to the Copyright Clearance Center, Inc., 222 Rosewood Drive, Danvers, MA 01923; include the code 0887-8722/07 $10.00 in correspondence with the CCC.

*Advisory Engineer, Applied Thermal Technologies, LLC, 2700 Via Fortuna, Suite 301, Austin, TX 78746; rice@athermal.com.

†United Technologies Endowed Chair Professor in Thermal-Fluids Engineering, Department of Mechanical Engineering, 191 Auditorium Road, Unit 3139; faghri@engr.uconn.edu.

variables over the thermophysical variables, to determine the condition in which their model is valid.

Leong et al. [5] developed an analytical model to capture the variation of the vapor pressure distribution of a flat-plate heat pipe. They solved the problem using a stream function that is calculated as the product of two functions, each a function of an orthogonal coordinate direction. They solved the pressure distribution for a FPHP with a symmetric heat source and heat sink and an asymmetric heat source and heat sink. Their model only considered the vapor region.

Wang and Vafai [6,7] experimentally and analytically characterized the transient characteristics during startup and shutdown operations for an asymmetrical flat-plate heat pipe. They found that the main thermal resistance in the heat pipe is from the wick, and that the thermal diffusivity, the wall and wick thickness, and the heat input pattern all affect the time constant to steady-state operation. Experimental work by Wang and Vafai [8] demonstrated that the temperature difference within a flat-plate heat pipe is small.

Xuan et al. [9] investigated flat-plate heat pipe performance by experimentally varying parameters such as heat flux, thickness of the wick, orientation, and fluid charge in the heat pipe. Their heat pipe design needed gravity to return the condensate to the evaporator. Esarte and Dominguez [10] experimentally studied a flat heat pipe working against gravity. In their heat pipe, the condensate was returned to the bottom of the heat pipe by gravitational forces, and then pumped up the evaporator by capillary action against gravity. They captured heat flowing from a large surface (evaporator) to a narrower one (condenser).

Tan et al. [11] considered the liquid flow and pressure field in an isotropic wick structure of a flat-plate heat pipe with multiple heat sources. They optimized the points of the heat sources by minimizing the maximum pressure distribution within the wick structure. Vadakkan et al. [12] also studied the transport characteristics in a flat heat pipe from multiple heat sources. They used a three-dimensional model which accounted for the wall, wick, and vapor core simultaneously. The evaporation/condensation rates were locally calculated using kinetic theory which needed an empirical constant (accommodation coefficient) with an overall energy balance at the liquid/vapor interface.

Because it is possible to obtain the pressure distribution within the wick structure, it is important to consider the maximum capillary pressure the wick structure can hold. Originally, Potash and Wayner [13] studied evaporation from an extended meniscus. The pressure gradients that drive the flow in the thin film included the disjoining pressure effects. Holm and Goplen [14] also studied the evaporation heat transfer in the thin-film region. They divided the heat transfer effects into three main regions: the evaporating film, the intrinsic meniscus, and the convection to the liquid where there is no change in curvature. All of the regions were solved separately and were idealized for a perfectly flat wall. Krustalev and Faghri [15] studied thin-film evaporation by not distinguishing any regions and also considering surface roughness effects. Ma et al. [16] studied the wicking height against gravity for different height inputs. They found that greater heat inputs, and therefore higher mass flow rates, caused an increase in contact angle and therefore a decrease in an effective capillary pressure.

The purpose of the present investigation is to develop a numerical model that can be used for cylindrical heat pipes as well as flat heat pipes, to solve the flow and pressure fields in the wick and the vapor core, and the thermal field in the wall, wick, and vapor core. This model can be used in two- and three-dimensional geometries. The model uses no empirical correlations to determine the mass flux across the liquid/vapor interface. Also, the reduction of the maximum effective capillary pressure due to the mass flux across the liquid/vapor interface is considered by a single pore analysis.

## II. Numerical Model

A general schematic of a cylindrical heat pipe is presented in Fig. 1. A heat source(s) is applied to one end of the heat pipe, and a heat sink is applied to the other. The vapor flows from the heat source to the heat sink in the vapor core and the liquid flows from the heat sink (condenser) to the heat source (evaporator). The evaporation and condensation processes provide the pressure gradient to drive the flow in the vapor core, whereas the pressure gradient in the wick is caused by the capillarity. The numerical model used divides the heat pipe into three regions: the solid wall, the wick, and the vapor core. These regions are solved as a single, coupled system. The heat sink at the outer wall is modeled in one of four ways: with a heat transfer coefficient, with a radiation heat sink, with a uniform heat sink, or by directly modeling the coolant flow through the jacket. Both high-temperature heat pipe (HTHP) and low-temperature heat pipes (LTHP) are modeled; the schematics for the HTHP and LTHP are presented in Figs. 1a and 1b. The equivalent flat-plate heat pipe is considered to be a cylindrical heat pipe that is unraveled, while maintaining the same vapor core, wick, and wall thicknesses. Therefore a heat input to a cylindrical heat pipe is the same heat input to $2\pi r_0$ of width to a flat-plate heat pipe. The basic assumptions are that the flow is laminar, the vapor can be considered an ideal gas, and the wick is saturated.

In the vapor core, the continuity equation for a compressible flow is

$$\frac{\partial \rho}{\partial t} + \nabla \cdot \rho \mathbf{V} = 0 \tag{1}$$

The momentum equation is

$$\frac{\partial}{\partial t}(\rho \mathbf{V}) + \nabla \cdot (\rho \mathbf{V}\mathbf{V}) = -\nabla p + \nabla \cdot \boldsymbol{\tau} \tag{2}$$

where $\boldsymbol{\tau}$

$$\boldsymbol{\tau} = \mu(\nabla \mathbf{V} + \nabla \mathbf{V}^T) - \tfrac{2}{3}\mu(\nabla \cdot \mathbf{V})\mathbf{I} \tag{3}$$

The energy equation is

$$\frac{\partial}{\partial t}(\rho h) + \nabla \cdot (\rho \mathbf{V} h) = \frac{Dp}{Dt} + \nabla \cdot (k \nabla T) + \Phi \tag{4}$$

$$\Phi = \nabla \mathbf{V} : \boldsymbol{\tau} \tag{5}$$

$h$ is defined as

$$h = C_p(T - T_{\mathrm{ref}}) \tag{6}$$

The equation of state for a compressible flow is the ideal gas law.

$$\rho = \frac{p}{RT} \tag{7}$$

The ideal gas constant $R$ is the universal gas constant divided by the molecular weight.

In the wick structure, a volume averaging approach is employed. For $\Theta$, the volume averaged value is found by averaging that variable over $V$.

$$\langle \Theta \rangle = \frac{1}{V}\int_V \Theta \, \mathrm{d}V \tag{8}$$

$\varphi$ can be found by integrating a function that equals one in a void in the porous zone, and zero on the solid matrix of the porous zone. Therefore, all of the governing equations can be volume averaged. There is also the intrinsic average of a variable, which is the average of any variable, only over the volume of the fluid in the pore.

$$\langle \Theta \rangle_f = \frac{1}{V_f}\int_V \Theta \, \mathrm{d}V \tag{9}$$

The volume average of a variable and the intrinsic average of a variable are related by

$$\langle \Theta \rangle = \varphi \langle \Theta \rangle_f \tag{10}$$

In the governing equations, conservation of mass, momentum, and

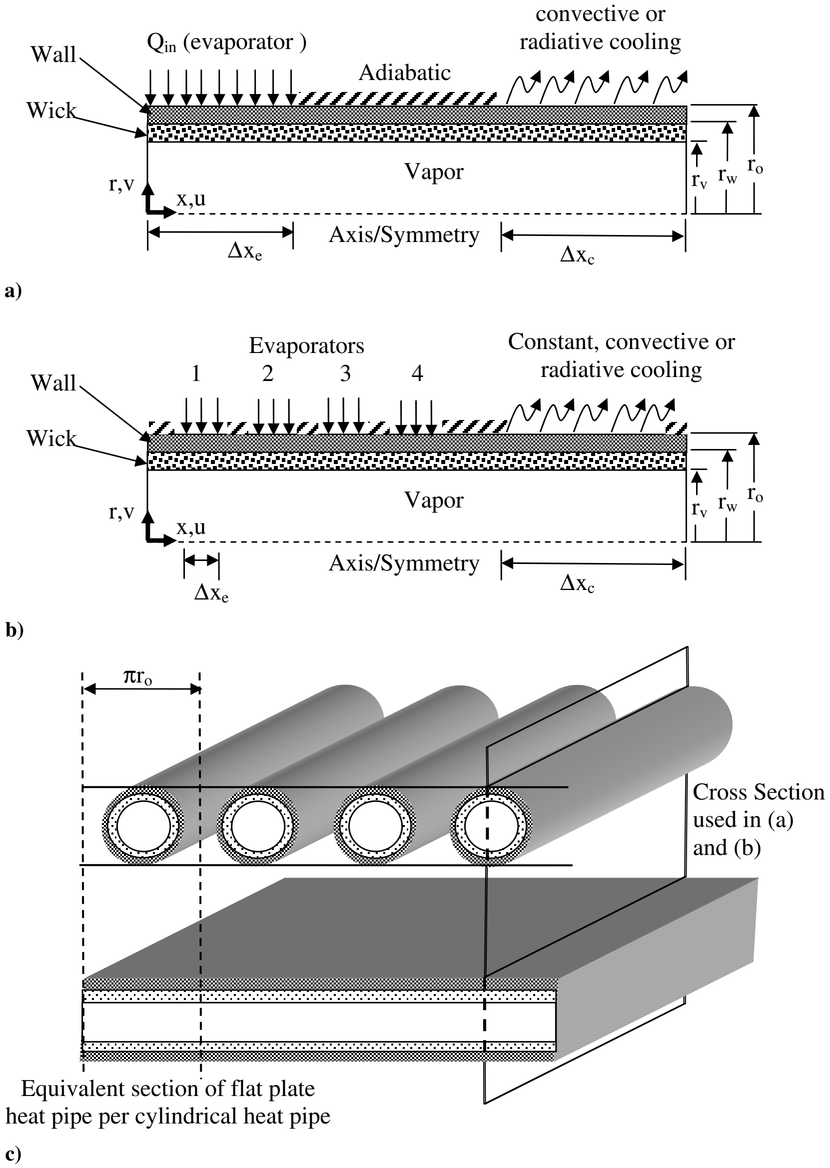

**Fig. 1 Side view of a a) high-temperature heat pipe, b) a low-temperature heat pipe with multiple heat sources, and c) the end view of a row of cylindrical heat pipes and an equivalent flat-plate heat pipe.**

energy, all of the deviations from the volume averaged variables as well as the products of deviation are considered to be negligible. Because the porous zone is assumed to be saturated with liquid, the volume averaged incompressible continuity equation for a single phase in a porous zone is

$$\nabla\cdot\varphi\langle\mathbf{V}\rangle_f = 0 \tag{11}$$

When the momentum equation is volume averaged, and the viscous interaction between the fluid and the solid matrix is modeled by a Darcy's law component and an inertial drag component, the momentum equation becomes

$$\begin{aligned}\frac{\partial}{\partial t}(\varphi\rho\langle\mathbf{V}\rangle_f) + \nabla\cdot(\varphi\rho\langle\mathbf{V}\rangle_f\langle\mathbf{V}\rangle_f) &= -\varphi\nabla p + \mu\nabla^2\langle\mathbf{V}\rangle_f \\ &\quad - \frac{\mu}{\mathbf{K}}\varphi^2\langle\mathbf{V}\rangle_f - \frac{f}{\mathbf{K}^{1/2}}\rho\varphi^3|\langle\mathbf{V}\rangle_f|\langle\mathbf{V}\rangle_f\end{aligned} \tag{12}$$

The wick porosity and the permeability are functions of the mesh number $N$ and the screen wired diameter $d$ for a screen wick [1]. The Ergun coefficient $f$ is 0.55.

$$\varphi = 1 - \frac{\pi S N d}{4} \tag{13}$$

$$\mathbf{K} = \frac{d^2\varphi^3}{122(1-\varphi)^2} \tag{14}$$

The volume averaged energy equation in a porous zone is

$$\frac{\partial(\rho h)_{\text{eff}}}{\partial t} + \nabla\cdot(\varphi\rho\langle\mathbf{V}\rangle_f\langle h\rangle_f)_l = \nabla\cdot k_{\text{eff}}\nabla\langle T\rangle \tag{15}$$

where

$$(\rho h)_{\text{eff}} = \varphi(\rho h)_f + (1-\varphi)(\rho h)_s \tag{16}$$

and

$$k_{\text{eff}} = \frac{k_f[k_f + k_s - (1-\varphi)(k_f - k_s)]}{k_f + k_s + (1-\varphi)(k_f - k_s)} \tag{17}$$

The liquid and the solid wick are assumed to be in local thermal equilibrium.

In the solid wall, only conduction heat transfer is solved; therefore the energy equation in the solid wall is

$$\frac{\partial \rho h}{\partial t} = \nabla \cdot (k \nabla T) \tag{18}$$

## III. Boundary Conditions

At a heated section on the outer wall

$$\left( r = r_0, x_{h,m} - \frac{\Delta x_h}{2} \le x \le x_{h,m} + \frac{\Delta x_h}{2} \right)$$

a constant heat flux is applied.

$$k_s \nabla T \cdot \mathbf{n}_s = \frac{\dot{Q}_{\text{in}}}{2\pi r_o (\Delta x_h)} \tag{19}$$

The unit normal vector $\mathbf{n}_s$ is pointing out of the solid wall. At the outer wall of the condenser section

$$\left( r = r_0, x_{c,m} - \frac{\Delta x_c}{2} \le x \le x_{c,m} + \frac{\Delta x_c}{2} \right)$$

the boundary conditions for convection, radiation, uniform heat sink, and direct simulation are

$$\text{Convection (heat transfer coefficient):} \; -k_s \nabla T \cdot \mathbf{n}_s = \lambda (T - T_\infty) \tag{20a}$$

$$\text{Radiation:} \; -k_s \nabla T \cdot \mathbf{n}_s = \sigma \varepsilon T^4 \tag{20b}$$

$$\text{Uniform heat sink:} \; -k_s \nabla T \cdot \mathbf{n} = \frac{\dot{Q}_{\text{tot}}}{2\pi r_o (\Delta x_c)} \tag{20c}$$

$$\text{Convection (directly):} \; -k_s \nabla T \cdot \mathbf{n}_s = k_c \nabla T \cdot \mathbf{n}_c \tag{20d}$$

The unit normal vector $\mathbf{n}_c$ is pointing into the solid wall. $\sigma$ is 5.6703$e$-8 w/m$^2 \cdot$ K$^4$. The emmissivity is denoted by $\varepsilon$. The outer section that is not heated or cooled is adiabatic ($r = r_0$, $x \ne x_c$, $x \ne x_h$).

$$\nabla T \cdot \mathbf{n}_s = 0 \tag{21}$$

At the interface between the outer wall, and the wick ($r = r_w$), the thermal boundary condition is

$$-k_s \nabla T \cdot \mathbf{n}_s = k_{\text{eff}} \nabla T \cdot \mathbf{n}_w \tag{22}$$

Also, all of the components of velocity in the wick are zero at the interface between the outer wall and the wick.

$$\mathbf{V} = 0 \tag{23}$$

The end caps of the heat pipe are adiabatic in the outer wall, wick and vapor sections.

$$\nabla T \cdot \mathbf{n}_{s,w,v} = 0 \tag{24}$$

In the vapor and wick, the velocity is zero at the end caps.

$$\mathbf{V}_v = \langle \mathbf{V}_l \rangle_f = 0 \tag{25}$$

The boundary conditions at a plane of symmetry or an axis are

$$\mathbf{V} \cdot \mathbf{n} = 0 \tag{26}$$

$$\nabla \mathbf{V} \cdot \mathbf{t} \cdot \mathbf{n} = 0 \tag{27}$$

### A. Wick/Vapor Interface

Special considerations need to be accounted for when considering the interface between the wick and the vapor region because the vapor interacts with the liquid in the wick's pores and the solid wick itself. Figure 2a is a schematic of the vapor/wick interfacial region. Because the scale of the individual liquid/vapor interface is small, the wick/vapor interface is assumed to be a plane at the inner edge of the wick r$_v$. The conservation of mass at the wick/vapor interface is

$$\dot{m}'' = -\rho_v \mathbf{V}_v \cdot \mathbf{n}_v = \varphi \rho_l \langle \mathbf{V}_l \rangle_f \cdot \mathbf{n}_l \tag{28}$$

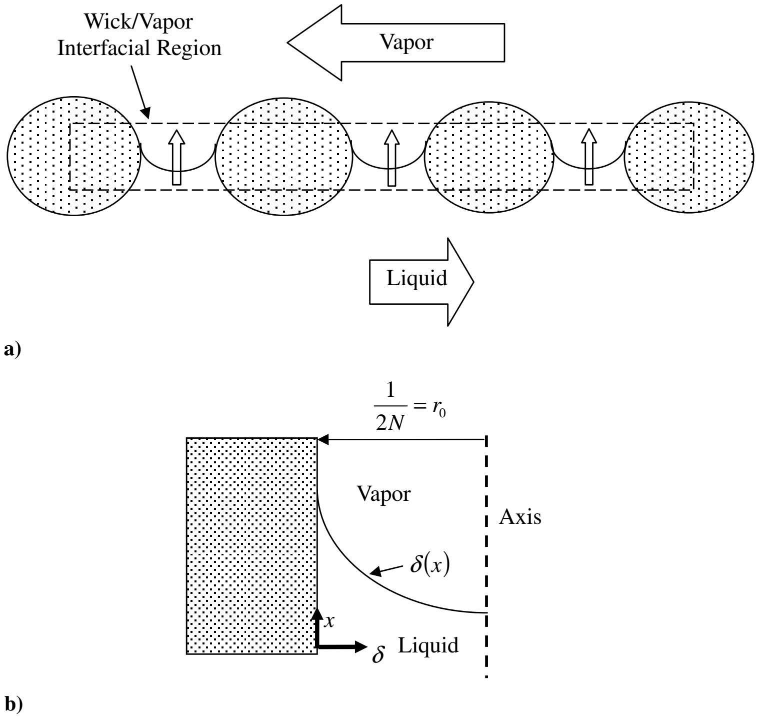

Fig. 2 Schematic of a) a wick/liquid/vapor interfacial region and b) and an idealized single pore.

The mass flux is

$$\dot{m}'' = (-k_{\mathrm{eff}} \nabla T \cdot \mathbf{n}_w - k_v \nabla T \cdot \mathbf{n}_v)/h_{\mathrm{fg}} \tag{29}$$

The interfacial energy balance is a more accurate representation than the interfacial energy balance previously used by Cao and Faghri [3] and by Vadakkan et al. [12]. They both included the sensible heat, however, they did not consider that the latent heat occurs at a reference temperature and not at absolute zero.

$$\dot{m}'' = \frac{(-k_{\mathrm{eff}} \nabla T \cdot \mathbf{n}_w - k_v \nabla T \cdot \mathbf{n}_v)}{h_{\mathrm{fg}} + (c_{p,v} - c_{p,l}) T_{\mathrm{sat}}} \tag{30}$$

The sensible heat is not presently included, because the enthalpy of both the liquid and the vapor is already accounted for in the latent heat of vaporization.

The tangential velocity of the vapor is zero at the interface because of the interaction with the solid wick. Also, the only component of the liquid velocity at the wick/vapor interface is assumed normal to the interface, therefore

$$\mathbf{V}_v \cdot \mathbf{t} = \langle \mathbf{V}_l \rangle_f \cdot \mathbf{t} = 0 \tag{31}$$

The momentum balance in the normal direction is not balanced as part of the solution procedure, but needs to be included to check if the wick has enough pumping potential to prevent capillary dry out. Because the interface is considered stationary, and the wick is considered completely saturated, the local normal momentum equation is

$$p_v - p_l - \dot{m}''(\mathbf{V}_l - \mathbf{V}_v) = \frac{2\sigma_{lv}}{r_{\mathrm{eff}}} = p_c \tag{32}$$

Even though the normal momentum equation is not balanced as part of the solution procedure, it can be used to check for operating limitations, such as capillary dry out. More discussion of this boundary condition is presented in Sec. IV. The interfacial temperature is equivalent to the saturation temperature. The saturation temperature is found by using the Clausius–Clapeyron equation.

$$T_I = T_{l,I} = T_{v,I} = T_{\mathrm{sat}} = \left( \frac{1}{T_0} - \frac{R}{h_{\mathrm{fg}}} \ln \left( \frac{P_v}{P_0} \right) \right)^{-1} \tag{33}$$

The saturation temperature is based on the vapor pressure at the wick/vapor interface. The liquid/vapor interface is assumed to have no thickness; therefore the liquid and vapor temperatures are both equal to the saturation temperature. Also, the effects of the pressure drop across the interface can be neglected because the order of magnitude of this pressure difference has a negligible effect on the accuracy of the results.

The governing momentum and energy equations are second order; therefore, two interfacial conditions for each component of momentum and energy are needed. The pressure is first order in the governing equations and therefore does not need to be specified at the interface. These criteria are met by Eqs. (28), (31), and (33); therefore the interfacial conditions are well posed.

### B. Operating Pressure of the System

The operating pressure is fixed when the condenser section is modeled using a constant heat sink, Eq. (20c). For the other cooling modes of the condenser, Eqs. (20a), (20b), and (20d), the operating pressure is directly related to the temperature of the heat sink at the condenser section. To let the operating pressure of the system float, so that it can be governed by the physics, the boundary condition at the end of the vapor core closest to the condenser, Eq. (23), can be relaxed and can be considered a pressure boundary. Also, assume that the pressure gradient, tangential to the surface, is negligible; therefore the pressure at this end can be considered constant.

$$\nabla p \cdot \mathbf{t} = 0 \tag{34}$$

Because a pressure boundary is used, mass will be able to enter or leave the vapor region, if the correct pressure is not used. To reduce the flow rate at this boundary an iterative procedure is used. The mass flow rate out of the vapor region can be approximated by

$$\dot{m}_{\mathrm{out}} = \frac{\dot{Q}_{\mathrm{in}} - \dot{Q}_{\mathrm{stor}} - \dot{Q}_{\mathrm{out}}}{h_{\mathrm{fg}}} \tag{35}$$

The heat rate into the heat pipe is specified and the mass flow rate out of the heat pipe needs to go to zero. To do this, we can control the system temperature, which will create a step change in the storage and the heat out of the system that will force the mass out of the system to go to zero.

$$\dot{m}_{\mathrm{out}} h_{\mathrm{fg}} = \Delta \dot{Q}_{\mathrm{stor}} + \Delta \dot{Q}_{\mathrm{out}} \tag{36}$$

For a steady-state solution, the storage rate term in Eq. (36) is not needed. For a steady-state solution, Eq. (36) can be satisfied by changing the temperature of the system by an increment:

$$\text{Convection heat sink}: \Delta T = \frac{\dot{m}_{\mathrm{out}} h_{\mathrm{fg}}}{A_c \lambda} \tag{37a}$$

$$\text{Radiation heat sink}: \Delta T = \left( \frac{\dot{m}_{\mathrm{out}} h_{\mathrm{fg}}}{A_c \sigma \varepsilon} + T_{\mathrm{ref}}^4 \right)^{1/4} - T_{\mathrm{ref}} \tag{37b}$$

If $\lambda$ is not known because of direct simulation of the coolant flow, it can be calculated by

$$\lambda = \frac{1}{A_c} \int_{A_c} \frac{\dot{Q}''_{\mathrm{out}}}{T_w - T_{\mathrm{in,coolant}}} \, \mathrm{d}A \tag{38}$$

The reference temperature in the radiation equation is calculated by

$$T_{\mathrm{ref}} = \left( \frac{\dot{Q}_{\mathrm{out}}}{A_c \sigma \varepsilon} \right)^{\frac{1}{4}} \tag{39}$$

To raise the system temperature by $\Delta T$, the new pressure of the right end cap in the vapor core is

$$p_{\mathrm{ec}} = p_0 \exp \left[ \frac{h_{\mathrm{fg}}}{R} \left( \frac{1}{T_0} - \frac{1}{T_{\mathrm{ec}} + \Delta T} \right) \right] \tag{40}$$

where $p_{\mathrm{ec}}$ is the new pressure of the end cap and $T_{\mathrm{ec}}$ is the old temperature of the end cap. Because a temperature gradient could exist on the end cap, the temperature $T_{\mathrm{ec}}$ is taken at the intersection of the end cap and the wick/vapor interface.

For unsteady solutions, the thermal capacity $TC$ of the heat pipe must be known.

$$TC = \int_{V_s} \rho_s C_{p,s} \, \mathrm{d}V + \int_{V_w} \varphi \rho_l C_{p,l} + (1 - \varphi) \rho_s C_{p,s} \, \mathrm{d}V + \int_{V_v} \rho_v C_{p,v} \, \mathrm{d}V \tag{41}$$

When a convective boundary is used, the temperature increase can be found by

$$\Delta T = \dot{m}_{\mathrm{out}} h_{\mathrm{fg}} \left( A_c \lambda + \frac{TC}{\Delta t} \right)^{-1} \tag{42}$$

where $\Delta t$ is the size of the current time step. The temperature increase is plugged into Eq. (40), to find the new pressure at the right end of the vapor core. For an unsteady radiation problem, there is no explicit solution to find the temperature increase because of the temperature raised to the fourth power. Therefore, the function $F(\Delta T)$ has to equal zero, so that the overall energy balance is met, and considering, $\dot{Q}_{\mathrm{out,rad}} = \varepsilon A \sigma (T_{\mathrm{ref}} + \Delta T)^4$.

$$F(\Delta T) = a_0 + a_1 \Delta T + a_2 \Delta T^2 + a_3 \Delta T^3 + a_4 \Delta T^4 \tag{43}$$

where the constants are equal to

$$a_0 = -\dot{m}_{\text{out}} h_{\text{fg}} \tag{44a}$$

$$a_1 = 4A_c \sigma \varepsilon T_{\text{ref}}^3 + \frac{TC}{\Delta t} \tag{44b}$$

$$a_2 = 6A_c \sigma \varepsilon T_{\text{ref}}^2 \tag{44c}$$

$$a_3 = 4A_c \sigma \varepsilon T_{\text{ref}} \tag{44d}$$

$$a_4 = A_c \sigma \varepsilon \tag{44e}$$

Newton's method is used to find this value.

$$\Delta T_{n+1} = \Delta T_n - \frac{F(\Delta T_n)}{F'(\Delta T_n)} \tag{45}$$

The convergence of this problem is considered when the relative change in the temperature increase is less than $1e-5$. Once the temperature increase is found, the new pressure at the boundary can be found by plugging this value into Eq. (39).

A colocated finite volume approach is used to discretize the governing equations. A pressure staggering scheme is used to interpolate the pressure in the same manner as a staggered mesh. The SIMPLE algorithm is used to introduce pressure into the continuity equation. The general numerical solution procedure is as follows:

1) Update pressure at end cap using Eq. (40).

2) Update fluid properties based on current solution, or initialize the solution.

3) Solve momentum equations.

4) Solve continuity (pressure correction equation).

5) Solve energy.

6) Repeat 2–5 until converged, then go to 1, if mass out is less than $Q_{\text{tot}}/5000h_{\text{fg}}$, than go to the next time step, or a steady solution is converged.

## IV. Reduction of Capillary Pressure Because of Mass Flux

A limiting analysis of the reduction of the capillary pressure due to the increased resistance of the liquid film for high heat fluxes is performed. In this analysis, the pressure gradient needed to drive the flow to the microfilm region is created by the change in surface curvature. Once the disjoining pressure effects are relevant, it is assumed that an unlimited pressure gradient can be achieved. The effective pore radius $r_0$ in a screen mesh wick is given in Faghri [1].

$$r_0 = \frac{1}{2N} \tag{46}$$

The screen mesh number is $N$. The effective pore radius can be used to calculate the static capillary pressure $p_{c,\text{static}}$.

$$p_{c,\text{static}} = \frac{2\sigma_{lv}}{r_0} \tag{47}$$

If there is no flow within a capillary tube, the effective capillary pressure $p_{c,0}$ is equivalent to the static capillary pressure. However as shown by Ma et al. [16], the mass flow rate in a capillary tube can also affect the effective capillary pressure. In the thin-film region, a large pressure gradient is needed to drive the flow because of the large shear losses. The pressure gradient is cause by the change in surface curvature and because of disjoining pressure effects. It is also known that most of the evaporation occurs in the thin-film region, as shown by Potash and Wayner [13], Holm and Goplen [14], and Khrustalev and Faghri [15]. To practically know how the effective radius of curvature is known, a key question is posed, *at what film thickness will the mass flow rate significantly be reduced by evaporation, and at this point, what is the major cause of the pressure gradient driving the flow*? From previous investigations, the mass flow rates are significantly reduced in the region where the change in surface curvature and the disjoining pressure effects both have comparable magnitudes in the pressure gradients. To find when this answer is possible, an idealized pore is used, as presented in Fig. 2b. The idealized pore is assumed to have a radius of $r_0$ and also to be cylindrical in shape.

The disjoining pressure can be modeled by an equation presented by Holm and Goplen [14].

$$p_d = \rho_l R T_\delta \ln\left[a\left(\frac{\delta}{3.3}\right)^b\right] \tag{48}$$

The disjoining pressure has a negligible effect when $p_d$ is equal to zero. At this value the film thickness is

$$\delta_d = 3.3\left(\frac{1}{a}\right)^{1/b} \tag{49}$$

If an analysis is performed, where the mass flow rate is assumed constant, and a pressure gradient produced by the change in curvature of a surface drives the flow, the minimum film thickness must be less than $\delta_d$, for the solution to be physically realistic. If the film thickness is greater than $\delta_d$, it will be impossible for the liquid to be pumped to the nonevaporating film thickness. Because a single pore is idealized as a cylindrical pore with radius $r_0$, the pressure drop across this liquid vapor interface is

$$p_c = p_v - p_l = -\sigma\left(\frac{-\delta''}{(\delta'^2+1)^{3/2}} - \frac{1}{(r_0-\delta)\sqrt{\delta'^2+1}}\right) \tag{50}$$

The vapor pressure can be considered constant, and therefore the change in the capillary pressure is equivalent to the change in the liquid pressure. To find the pressure gradient needed, the shear stress must be known at the wall. The shear stress can be found by knowing the fluid Poiseuille $Po$ number.

$$Po = C_f\,Re_\delta = \frac{\tau_w}{0.5\rho_l \bar{u}^2}\frac{\rho_l \bar{u}\delta}{\mu_l} = 6 \tag{51}$$

The pressure gradient for a flow in which the inertial effects are assumed to have a negligible effect is

$$\frac{\mathrm{d}p_c}{\mathrm{d}x} = \frac{2r_0\tau_w}{(2r_0-\delta)\delta} \tag{52}$$

The mass flow rate is considered constant throughout this analysis, because the evaporative effects are not yet important, therefore through continuity, the average velocity $\bar{u}$ is

$$\bar{u} = \frac{u_0 r_0^2}{(2r_0-\delta)\delta} \tag{53}$$

where the initial velocity is

$$u_0 = \frac{\dot{m}_{\text{pore}}}{\rho_l \pi r_0^2} \tag{54}$$

The mass flow rate in a pore can be calculated by the average heat input to a single pore by

$$\dot{m}_{\text{pore}} = \frac{Q_{\text{tot}}}{h_{\text{fg}} N^2 A_h} \tag{55}$$

where $Q_{\text{tot}}$ is the total heater power (watts) of one heater, $A_h$ is the area of that heater, and $N^{-2}$ is the total area of a single pore and its surrounding wick. By combining Eqs. (51–55), the pressure gradient is

$$\frac{\mathrm{d}p_c}{\mathrm{d}x} = \frac{6r_{\text{eff}}\mu_l}{(2r_{\text{eff}}-\delta)^2\delta^3}\frac{Q_{\text{tot}}}{\rho_l h_{\text{fg}} N^2 A_h} \tag{56}$$

Also Eq. (50) can be rearranged, so the second derivative of $\delta$ with respect to $x$ is

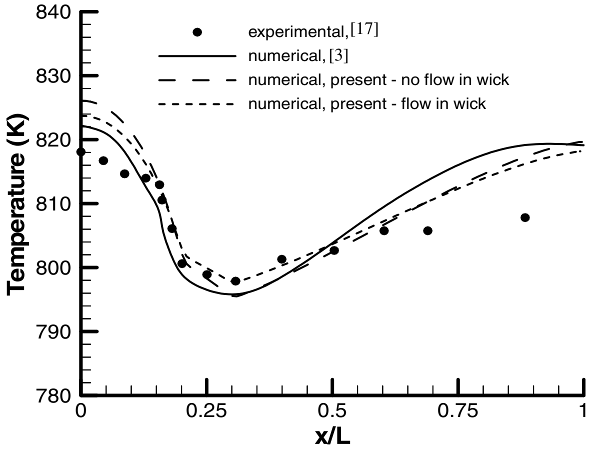

**Fig. 3 Centerline vapor temperature distribution, in a cylindrical HTHP.**

$$\delta'' = (\delta'^2 + 1)^{3/2}\left[\frac{p_c}{\sigma} - \frac{1}{(r_0 - \delta)\sqrt{\delta'^2 + 1}}\right] \tag{57}$$

Equations (55) and (56) can be solved numerically, with initial conditions:

$$\delta = 0.99999 r_0 \tag{58a}$$

$$\delta' = -1 \times 10^9 \tag{58b}$$

$$p_c = p_{c,0} \tag{58c}$$

The reason for the coefficient in front of Eq. (58a) is to prevent a singularity in Eq. (57). Also, a slope of $-\infty$ is numerically impossible, therefore, a very large negative number is used in Eq. (58b). Equations (56) and (57) can be solved with a variable-order solver based on the numerical differentiation formulas.

For each heat input (mass flow rate) for a single pore, with an associated effective capillary pressure $p_{c,0}$, the solution to Eqs. (56) and (57) will produce a minimum film thickness $\delta_{\min}$. If $\delta_{\min}$ is greater than $\delta_d$, then the overall capillary pressure is too large and needs to be reduced, because it is impossible to reach an equilibrium film thickness, because the disjoining pressure effects are not yet significant. If $\delta_{\min}$ is greater than $\delta_d$, then the disjoining pressure effects become significant, and it may be possible for the film to reach an equilibrium film thickness. Because of these two statements, the maximum effective capillary pressure for a given heat input is reached when $\delta_{\min}$ is equal to $\delta_d$.

## V. Results

The present numerical analysis is validated on several cases, for both low- and high-temperature operation. Also, the transient response for a pulsed heat input on a high-temperature heat pipe is considered. Multiple heater configurations are examined on a low-temperature heat pipe. The temperature distribution and maximum capillary pressure required to support these heating loads are examined. The capillary pressure needed, calculated from the full numerical simulation, is used along with the capillary pressure reduction analysis to predict the heating loads at which capillary dry

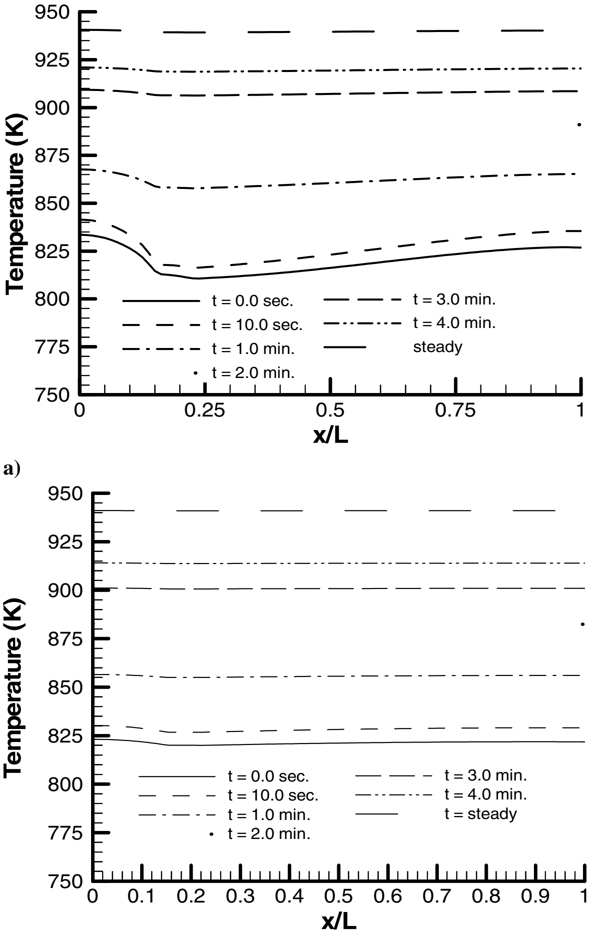

a)

b)

**Fig. 4 Present numerical results of centerline vapor temperature distribution in a HTHP response to step change in heat input with convective cooling in a a) cylindrical and b) a flat-plate configuration.**

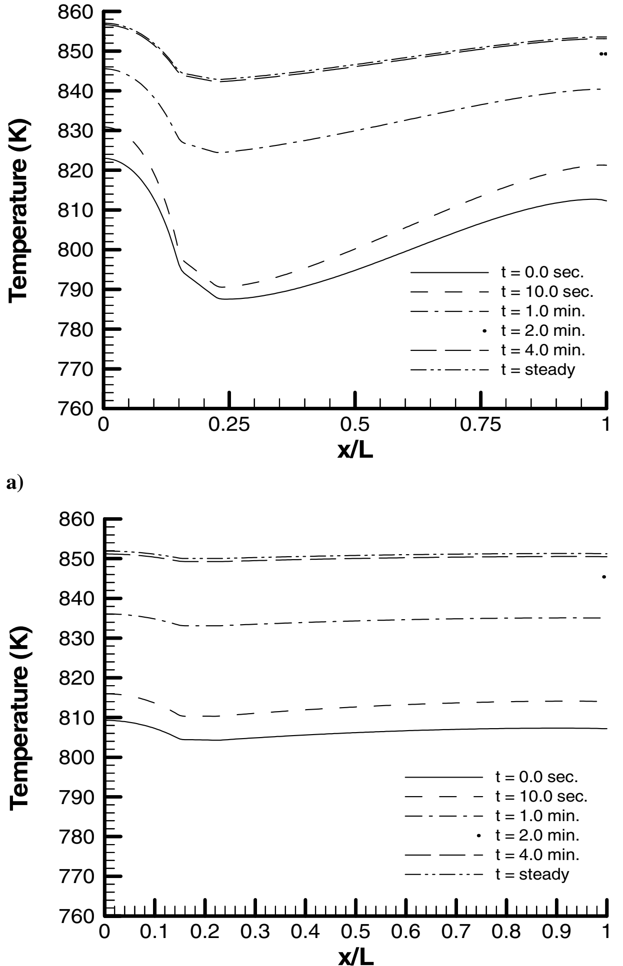

a)

b)

**Fig. 5 Present numerical results of centerline vapor temperature distribution in a HTHP response to step change in heat input with radiative cooling in a a) cylindrical and b) a flat-plate configuration.**

out will occur. These results are compared with experimental results of dry-out conditions. The mesh used for all cases had 15 cells in the vapor region between the axis/symmetry, to the wick/vapor interface. There were five cells across the wick and five cells across the solid. For the HTHP, the evaporator had 30 cells in the $x$ direction, 15 cells along the adiabatic section, and 150 cells, in the condenser section, for a total of 195 cells in the $x$ direction. For the LTHP, there were 10 cells modeled along each evaporator, 11 cells were modeled on the adiabatic sections between each evaporator, 42 cells along the condenser section, 37 cells between evaporator 4 and the condenser section, and 3 cells on the adiabatic section at the ends of the heat pipe for a total of 155 cells in the $x$ direction. On the HTHP, a grid study was performed on the validation case, where the cells across the vapor, wick, and solid regions were 10, 3, and 3, respectively, and the cells along the evaporator, adiabatic, and condenser section were 20, 10, and 70 cells, respectively. There was less than a 0.2% difference in temperature along the axis and along the outer wall, at every point. Also, there was less than a 0.2% difference in pressure along the axis at every point.

### A. High-Temperature Heat Pipes (HTHP)

The present numerical solutions for the steady operation of a cylindrical high-temperature sodium heat pipe are compared to the experimental results of Ivanovskii [17] and the numerical results of Cao and Faghri [3]. The results are presented in Fig. 3. The evaporator starts at $x = 0.0$, which is followed by an adiabatic section, and then a condenser section. The length of the evaporator, adiabatic, and condenser sections are 0.1, 0.05, and 0.35 m, respectively. The thicknesses of $r_v$, $r_w$, and $r_0$ are 0.007, 0.008, and 0.009 m, respectively. The heater power to the evaporator is 560 W, and the condenser is modeled by a convection boundary condition with a heat transfer coefficient of $58.5\ \mathrm{W/m^2 \cdot K}$, and a reference temperature of 300 K. When the flow in the wick is modeled, the advective thermal transport of the liquid sodium slightly reduces the maximum temperature and slightly increases the minimum temperature, but is generally insignificant, as assumed by Cao and Faghri [3]. The most significant difference between the present numerical results and their numerical results is that the interfacial energy balance is used for the entire interface in the present simulations. They only used the interfacial energy balance in the evaporator and adiabatic section, with an outflow type boundary with a latent heat source term in the condenser section.

The transient response of a high-temperature sodium filled heat pipe, with stainless steel walls is presented in Figs. 4–7. The evaporator, adiabatic, and condenser sections have a length of 0.105, 0.0525, and 0.5425 m, respectively. The thicknesses $r_v$, $r_w$, and $r_0$ have values of 0.007, 0.008, and 0.009 m, respectively. The condenser is modeled with a heat transfer coefficient of $39.0\ \mathrm{W/m^2 \cdot K}$, and a reference temperature of 300 K, for the convection type boundary, and for the radiative condition the emmissivity $\varepsilon$ is 0.85. The initial condition is the steady-state operation of a heat input of 623 W. The transient process starts when the heat input is increased to 770 W. The time step size was 5 s. A test run, where the time step size was reduced to 2.5 s, was simulated, and the temperature difference between the time steps for all times was less than 0.2%. The flow in the wick was not modeled for the transient cases for two reasons: it does not significantly affect the results, because continuity is violated if the wick is assumed saturated at all

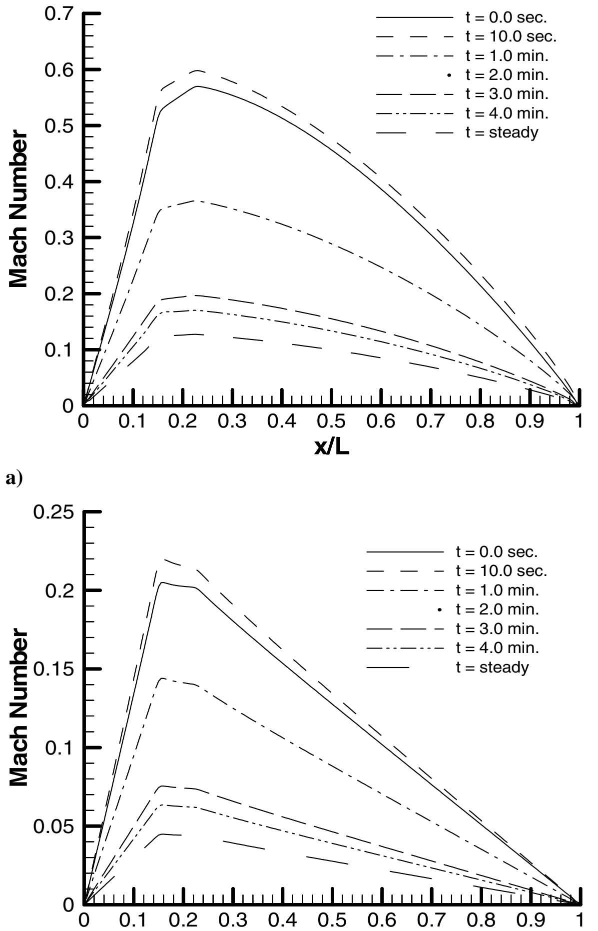

a)

b)

**Fig. 6 Centerline Mach number in the response of a HTHP under step change in heat input with convective cooling in a a) cylindrical and b) a flat-plate configuration.**

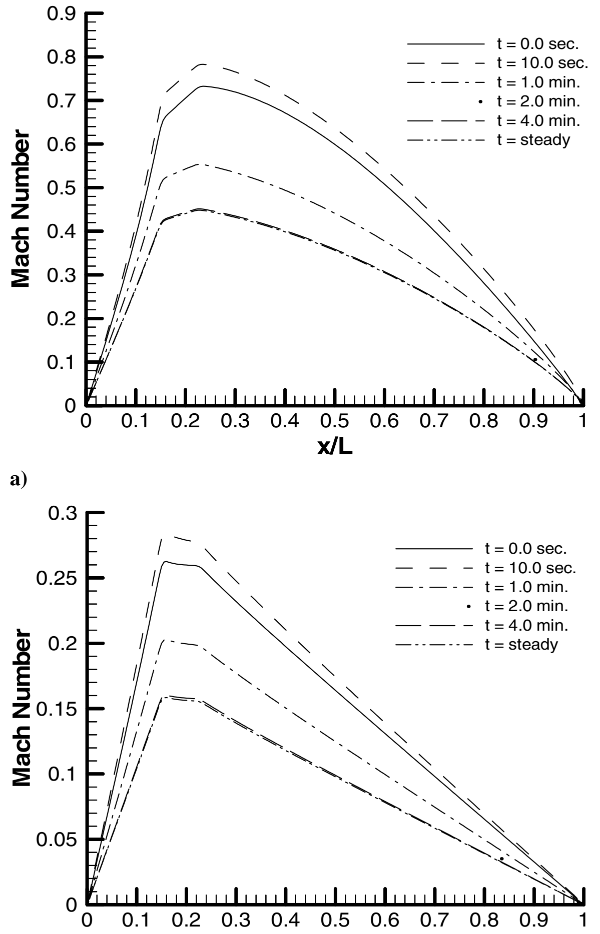

a)

b)

**Fig. 7 Centerline Mach number in the response of a HTHP under step change in heat input with radiative cooling in a a) cylindrical and b) a flat-plate configuration.**

times, and the condensation and evaporating rates differ, as is the present case. It is important to note that these are the only cases that neglect the flow in the wick.

The responses of a HTHP with convective cooling, in a cylindrical and flat-plate configuration, are compared in Fig. 4. The transient response of both systems is very similar; the only noticeable differences are that the cylindrical HTHP has a larger temperature drop than the flat-plate HTHP, at early times, which correspond to lower temperatures. Note that lower temperature directly means lower pressure because of the interfacial boundary condition, Eq. (33). The density is also lower at lower temperatures because of the logarithmic dependence of pressure on temperature, and the ideal gas law. This difference can be attributed to the difference in the magnitude of velocity, present as centerline Mach number in Fig. 6. The Mach number is generally higher in the cylindrical heat pipe than the flat-plate heat pipe, because the vapor core cross-sectional area per heat input is much smaller, causing higher velocities. However, as the density increases with temperature and time, the compressibility effects become negligible in the cylindrical heat pipe after 2.0 min, and the temperature profile flattens out significantly at this time and later. The compressibility effects are never important for the flat-plate configuration, and that is why the temperature profiles are much more uniform at all times.

The same behaviors for a HTHP with radiative cooling are observed as convective cooling in a cylindrical and flat-plate HTHP. The transient temperature profiles and Mach number profiles along the centerline are presented in Figs. 5 and 7, respectively. The major difference is that compressibility effects in the cylindrical heat pipe are prevalent at all times, because the radiative boundary can reject more heat than the convective boundary with a smaller temperature increase, because of the difference in the power of temperature of these two conditions.

### B. Low-Temperature Heat Pipes (LTHP)

The operation of a low-temperature heat pipe with multiple heat sources is examined. There are four heaters around the heat pipe with a length of 0.0635 m. The beginning of heaters 1, 2, 3, and 4 is at $x$ locations of 0.020, 0.1588, 0.2976, and 0.4364 m, respectively. The beginning of the condenser section is at an $x$ location of 0.680 m and it has a length of 0.300 m. The outer wall of the heater pipe that is neither heated nor cooled is adiabatic, and the total length of the heat pipe is 1.000 m. The thicknesses of $r_v$, $r_w$, and $r_0$ are 0.01025, 0.0110, and 0.0127 m, respectively. The operating fluid is water, and the outer wall and wick are copper. The screen mesh number $N$ of the wick is $1.97e3\ \mathrm{m}^{-1}$. To have a completely saturated wick, there needs to be a fluid fill of 34.5 g in the cylindrical heat pipe, and 41.3 g per $2\pi r_0$ m, in a flat-plate heat pipe.

The outer wall temperatures for different heating configurations of the present simulations compared to the experimental results of Faghri and Buchko [2] are presented in Fig. 8. The boundary condition at the condenser is a constant heat sink. The temperatures match up very closely, with the largest discrepancy in the condenser section. The origin of the disagreement of temperatures in the condenser section is because the condenser is cooled by water flowing in a cooling jacket. Therefore a 2-D–axisymmetric cooling

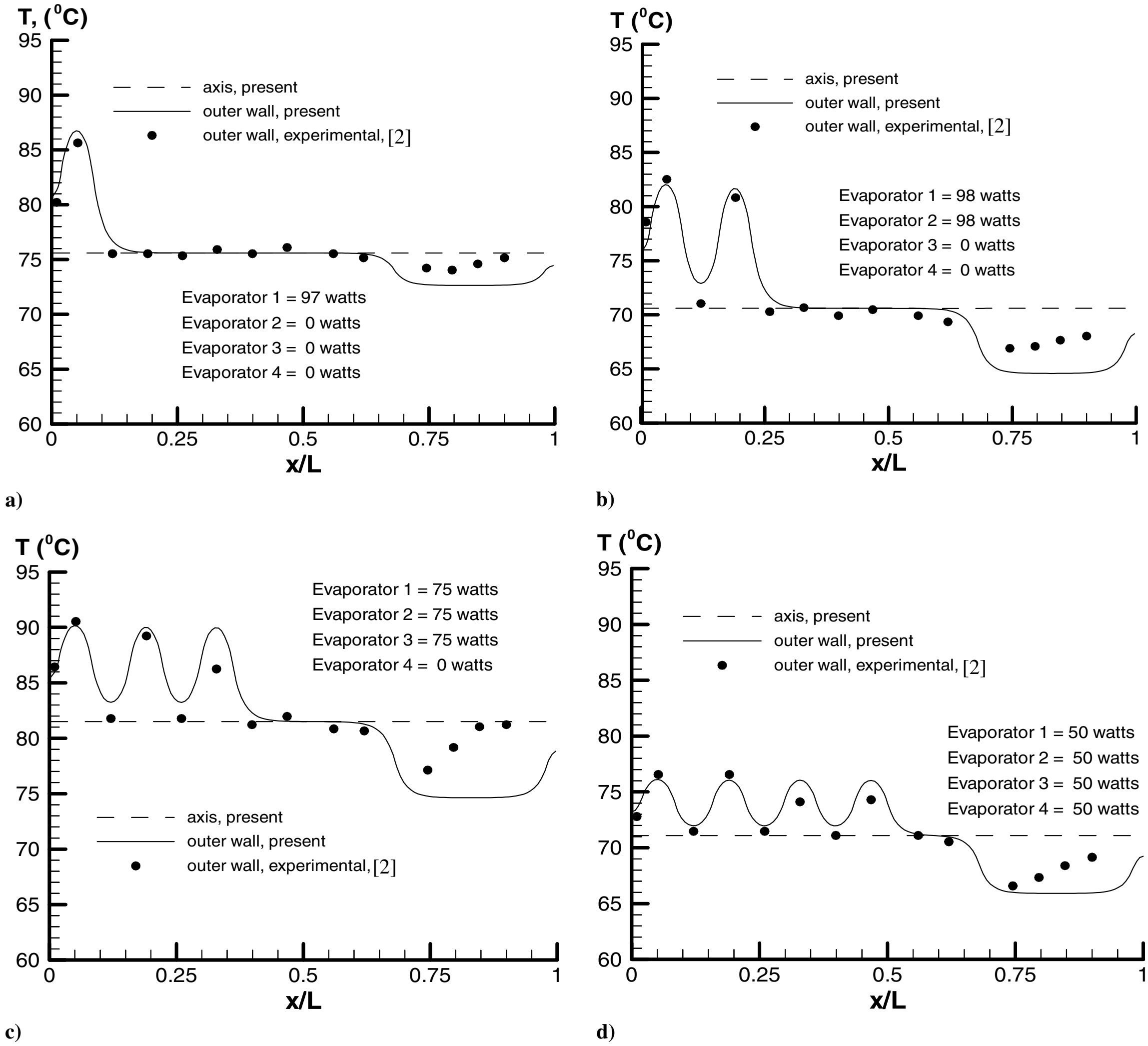

**Fig. 8 Comparison of experimental outer wall temperatures with present numerical simulations on a cylindrical LTHP with a constant heat sink for four different heating configurations.**

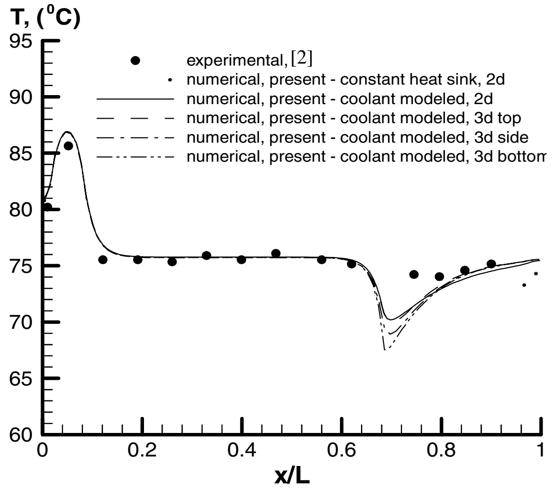

**Fig. 9 Comparison of different cooling boundary conditions on a cylindrical LTHP, with 97 W applied to evaporator 1, and 0 W applied to evaporators 2, 3, and 4.**

jacket is modeled, where the coolant uniformly enters and uniformly leaves the cooling jacket from either side in the circumferential direction. A 3-D simulation is also performed where the flow enters the top left portion of the cooling jacket and leaves the bottom right portion. The outer wall temperature profiles of these two cases are compared with experimental results and a constant heat sink boundary condition in Fig. 9. The operating temperature of the heat pipe was adjusted by changing the flow rate and inlet temperature of the coolant. By modeling the coolant flow, the temperature profile of the numerical simulations more closely matches the experimental results than the constant heat sink boundary condition. However, no flow rates or temperatures of the coolant flow are reported; therefore, a constant heat sink condition is applied for practical purposes for the rest of the LTHP cases. The centerline temperature is nearly constant because the pressure drop across the vapor region is very small, and the Mach number is also very small; therefore the results are not presented.

The same cases presented in Fig. 8 are run and compared to a flat-plate LTHP in Fig. 10. The outer wall temperature is slightly lower in the flat-plate heat pipes in the evaporator sections and slightly higher in the condenser section. This is due to the contraction of the surface area in cylindrical coordinates, causing higher heat flux across the wick, which has the highest thermal resistance, and therefore is where the highest temperature gradients occur.

### C. Reduction of Capillary Pressure and Capillary Dry Out of LTHP

The minimum film thickness produced by neglecting the disjoining pressure effects is presented versus heater power in Fig. 11a. If the minimum film thickness $\delta_{\min}$ is less than $\delta_d$, than the overall capillary pressure can support that heating load; if it is greater, than the overall capillary pressure cannot support the heating load. The maximum capillary pressure vs heating load is presented in

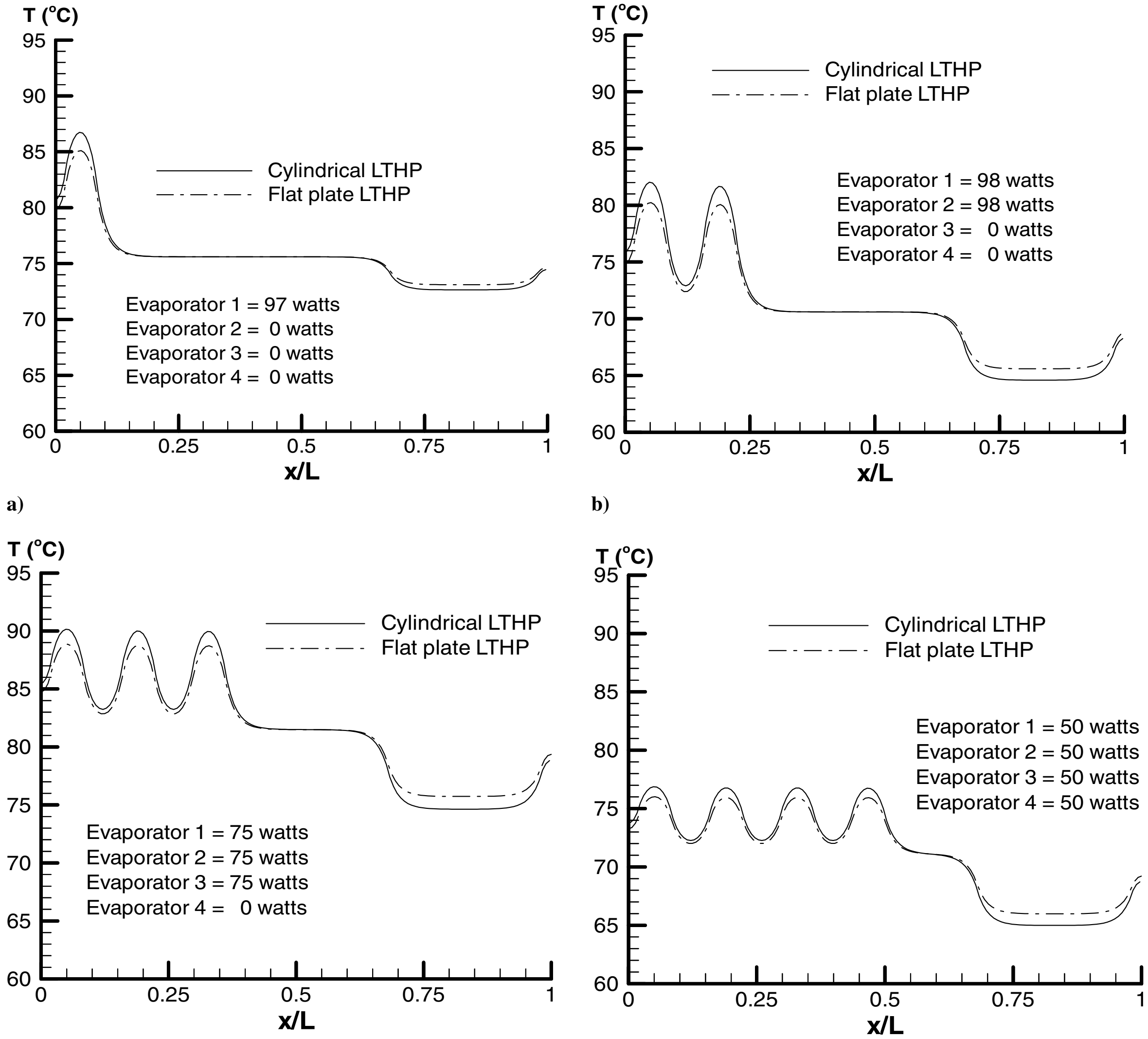

a) b) c) d)

**Fig. 10 Comparison of outer wall temperatures of a cylindrical heat pipe with the outer wall temperatures of an equivalent flat-plate heat pipe.**

Fig. 11b, which is the intersection of the root of disjoining pressure and the minimum film thickness, for different capillary pressure. For the heating loads in the present simulations, 100–400 W, the maximum capillary pressure is reduced by less than 5%.

To analyze the capillary dry-out limitations of a heat pipe, the pressure drop inside the wick must be known. The pressure drop $-p_c$ in the wick is needed to drive the flow. The difference in this pressure drop for different types of condenser boundary conditions is presented in Fig. 12a. The pressure drop in the wick is greatest for the constant heat sink boundary condition because the liquid has to flow the greatest distance. The magnitude of the condenser temperature drops from the adiabatic temperature in Fig. 9 indicates the region in which condensation occurs. For conservative approximations of the pressure drop in the wick structure, the value from the constant heat sink boundary conditions is taken for dry-out predictions. The difference in the overall pressure drop due to the condenser section boundary condition is approximately 15%. For a constant heat sink boundary condition, the pressure drops in a cylindrical LTHP and a flat-plate LTHP, with the same heating and cooling effects are compared in Fig. 12b. The pressure drop needed in the cylindrical heat pipe is greater than that of the flat heat pipe because of the difference in the cross-sectional area of wick per heat input.

For the 12 cases listed in Table 1, the total evaporator heat input $Q_{\mathrm{tot}}$ is increased by increments of 12.5 W, until that total capillary pressure drop between two points bounds the maximum capillary pressure presented in Fig. 11b. The condenser section is cooled by a constant heat sink boundary condition. From these points, the total maximum evaporator heat input to cause capillary dry out is interpolated. The maximum predicted total heater power is compared with the experimental dry-out limitations for a cylindrical LTHP. A large portion of the error is suspected to be attributed to the choice of the condenser section boundary condition (constant heat sink in these cases); however, the results still give a very good idea of when the capillary limit will be reached. Also the maximum heat input before dry out occurs in a flat-plate LTHP, also presented in Table 1. The average ratio of the maximum heat input for the flat-plate heat pipe compared to the cylindrical heat pipe is 1.21. This is also the ratio of the cross-sectional area of the wick of the flat-plate heat pipe to the cylindrical heat pipe.

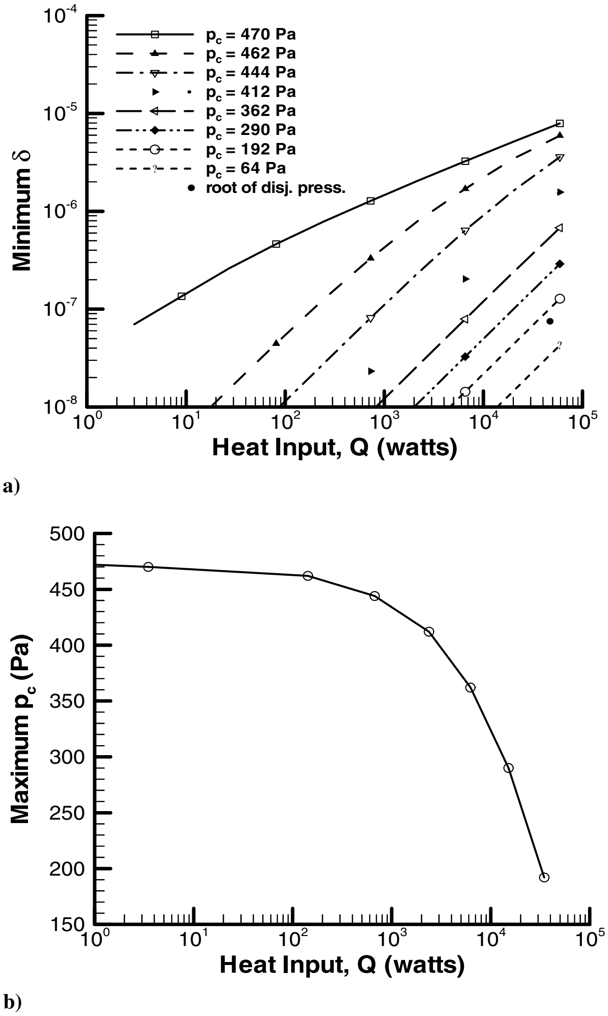

a)

b)

**Fig. 11 a) Minimum film thickness achieved with constant mass flow rate for different effective capillary pressures and b) the maximum effective capillary pressure as a function of the heat input.**

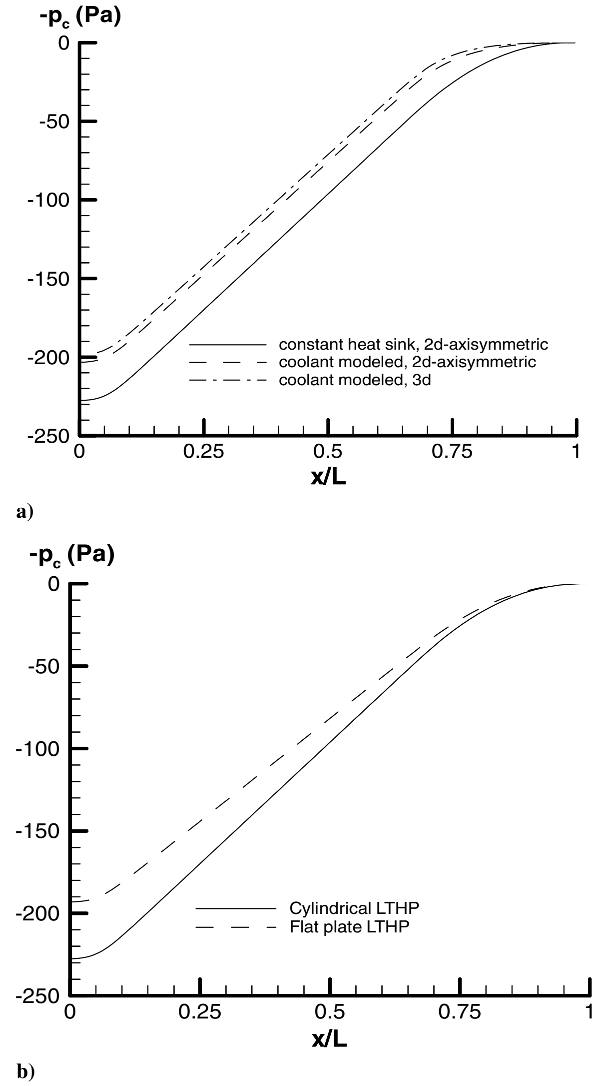

a)

b)

**Fig. 12 Comparison of the capillary pressure in present numerical simulations for 97 W applied to evaporator 1 in a a) cylindrical LTHP with different cooling conditions and in a b) cylindrical LTHP and a flat-plate LTHP with a constant heat sink cooling condition.**

## VI. Conclusions

A numerical model is presented that can predict the fluid mechanics and thermal transport characteristics for HTHPs and LTHPs. The model allows for the operating pressure of the system to be governed by the thermal cooling characteristics of the condenser. These characteristics are analyzed for cylindrical and flat-plate heat pipe geometries. From the analyses, several conclusions can be made as follows:

1) In HTHPs, the compressibility effects are not as important for flat-plate heat pipes as they are with cylindrical heat pipes because the vapor core cross-sectional area is greater.

**Table 1 Dry-out limitations of LTHP with multiple heat sources**

| | | | | | $Q_{\text{tot}}$, dry out, W | | | | |
|---|---|---|---|---|---|---|---|---|---|
| | Evaporator power | | | | Cylindrical | | | Flat plate | |
| Case | 1 | 2 | 3 | 4 | Experimental[a] | Present, numerical | % difference $100(\text{num.} - \text{exp.})/\text{exp.}$ | Present, numerical | $Q_{\text{flat plate}}/Q_{\text{cylindrical}}$ |
| 1 | $Q_{\text{tot}}$ | 0 | 0 | 0 | 181 | 186 | 2.76 | 223 | 1.20 |
| 2 | 0 | $Q_{\text{tot}}$ | 0 | 0 | >247 | 224 | N/A | 266 | 1.19 |
| 3 | 0 | 0 | $Q_{\text{tot}}$ | 0 | >246 | 281 | N/A | 333 | 1.18 |
| 4 | 0 | 0 | 0 | $Q_{\text{tot}}$ | >246 | 379 | N/A | 446 | 1.18 |
| 5 | $Q_{\text{tot}}/2$ | $Q_{\text{tot}}/2$ | 0 | 0 | 237 | 204 | −13.92 | 245 | 1.20 |
| 6 | $Q_{\text{tot}}/3$ | $Q_{\text{tot}}/3$ | $Q_{\text{tot}}/3$ | 0 | 334 | 225 | −32.63 | 272 | 1.21 |
| 7 | $Q_{\text{tot}}/4$ | $Q_{\text{tot}}/4$ | $Q_{\text{tot}}/4$ | $Q_{\text{tot}}/4$ | 392 | 252 | −35.71 | 305 | 1.21 |
| 8 | $Q_{\text{tot}}/2$ | 0 | $Q_{\text{tot}}/2$ | 0 | 321 | 226 | −29.60 | 271 | 1.20 |
| 9 | $Q_{\text{tot}}/2$ | 0 | 0 | $Q_{\text{tot}}/2$ | 299 | 255 | −14.72 | 304 | 1.19 |
| 10 | 100 | 0 | 0 | $Q_{\text{tot}} - 100$ | >342 | 282 | N/A | 363 | 1.29 |
| 11 | 100 | 0 | $Q_{\text{tot}} - 100$ | 0 | 350 | 233 | −33.43 | 294 | 1.26 |
| 12 | 100 | $Q_{\text{tot}} - 100$ | 0 | 0 | 284 | 204 | −28.17 | 251 | 1.23 |

[a] Experimental results from Faghri and Buchko [2].

2) A radiative boundary on a HTHP keeps the operating temperature of the heat pipe in a tighter range than a convective boundary for a heat increase.

3) The maximum effective capillary pressure of a single pore decreases as a function of heat input.

4) The capillary pressures of a LTHP needed to support steady-state operation can be determined for cylindrical and flat-plate heat pipe designs. These pressures can be compared to the computed maximum capillary pressures for given heat inputs, to determine the dry-out limitations of these heat pipes.

## References

[1] Faghri, A., *Heat Pipe Science and Technology*, Taylor and Francis, Washington, D.C., 1995.

[2] Faghri, A., and Buchko, M., "Experimental and Numerical Analysis of Low-Temperature Heat Pipes with Multiple Heat Sources," *Journal of Heat Transfer*, Vol. 113, 1991, pp. 728–734.

[3] Cao, Y., and Faghri, A., "Transient Two-Dimensional Compressible Analysis for High-Temperature Heat Pipes with Pulsed Heat Input," *Numerical Heat Transfer*, Vol. 18, 1990, pp. 483–502.

[4] Zuo, Z., and Faghri, A., "A Network Analysis of the Heat Pipe," *International Journal of Heat and Mass Transfer*, Vol. 41, No. 11, 1998, pp. 1473–1484.

[5] Leong, K. C., Liu, C. Y., and Sun, K. H., "Vapor Pressure Distribution of a Flat Plate Heat Pipe," *International Communications in Heat and Mass Transfer*, Vol. 23, No. 6, 1996, pp. 789–797.

[6] Wang, Y., and Vafai, K., "Transient Characterization of Flat Plate Heat Pipes During Startup and Shutdown Operations," *International Journal of Heat and Mass Transfer*, Vol. 43, 2000, pp. 2641–2655.

[7] Wang, Y., and Vafai, K., "An Experimental Investigation of the Transient Characteristics on a Flat-Plate Heat Pipe During Startup and Shutdown Operations," *Journal of Heat Transfer*, Vol. 122, 2000, pp. 525–535.

[8] Wang, Y., and Vafai, K., "An Experimental Investigation of the Thermal Performance of an Asymmetrical Flat Plate Heat Pipe," *International Journal of Heat and Mass Transfer*, Vol. 43, 2000, pp. 2657–2668.

[9] Xuan, Y., Hong, Y., and Qiang, L., "Investigation on Transient Behaviors of Flat Plate Heat Pipes," *Experimental Thermal and Fluid Science*, Vol. 28, 2004, pp. 249–255.

[10] Esarte, J., and Dominguez, M., "Experimental Analysis of a Flat Heat Pipe Working Against Gravity," *Applied Thermal Engineering*, Vol. 23, 2003, pp. 1619–1627.

[11] Tan, B. K., Huang, X. Y., Wong, T. N., and Ooi, K. T., "A Study of Multiple Heat Sources on a Flat Plate Heat Pipe Using a Point Source Approach," *International Journal of Heat and Mass Transfer*, Vol. 43, 2000, pp. 3755–3764.

[12] Vadakkan, U., Garimella, S. V., and Murthy, J. Y., "Transport in Flat Heat Pipes at High Heat Fluxes from Multiple Discrete Sources," *Journal of Heat Transfer*, Vol. 126, 2004, pp. 347–354.

[13] Potash, M., Jr., and Wayner, P. C., "Evaporation from a Two-Dimensional Extended Meniscus," *International Journal of Heat and Mass Transfer*, Vol. 15, 1972, pp. 1851–1863.

[14] Holm, F. W., and Goplen, S. P., "Heat Transfer in the Meniscus Thin-Film Transition Region," *Journal of Heat Transfer*, Vol. 101, 1979, pp. 543–547.

[15] Khrustalev, D., and Faghri, A., "Heat Transfer During Evaporation on Capillary-Grooved Structures of Heat Pipes," *Journal of Heat Transfer*, Vol. 117, 1995, pp. 740–747.

[16] Ma, H. B., Peterson, G. P., and Pratt, D. M., "Disjoining Pressure Effect on the Wetting Characteristics in a Capillary Tube," *Microscale Thermophysical Engineering*, Vol. 2, 1998, pp. 283–297.

[17] Ivanovskii, M. N., Sorokin, V. P., and Yagodkin, I. V., *The Physical Principles of Heat Pipes*, Oxford Univ. Press, Oxford, England, 1982.